LARGE-EDDY SIMULATION OF SINGLE-PHASE FLOW DYNAMICS AND MIXING IN AN INDUSTRIAL CRYSTALLIZER

J. J. Derksen[1]*, K. Kontomaris[2], J. B. McLaughlin[3] and H. E. A. Van den Akker[1]

[1]Multi-Scale Physics Department, Delft University of Technology, Delft, The Netherlands.
[2]DuPont Engineering Research and Technology, Experimental Station, Wilmington, Delaware, USA.
[3]Department of Chemical and Biomolecular Engineering, Clarkson University, Potsdam, New York, USA.

Abstract: The design of industrial crystallizers requires detailed information about the fine structure of turbulence in vessels of complex geometry. The currently available methods (e.g., empirical correlations, experimentation, simple theories, computations based on the Reynolds-averaged Navier–Stokes equations) cannot provide the required information at an adequate level of accuracy for crystallizers of non-standard design. This paper assesses the feasibility of using a computationally efficient large-eddy simulation (LES) technique to quantify the fine scale turbulent structure in an industrial crystallizer. LESs of the single-phase flow in a baffled, industrial crystallizer with a draft tube were performed at three values of the Reynolds number ($Re = 14\,000$, $Re = 82\,000$ and $Re = 350\,000$). The flow was driven by a standard Rushton turbine. A much weaker secondary flow was generated by a throughput stream that entered through a nozzle at the bottom and exited through the sidewall. The effects of the spatial resolution and the sub-grid scale model were investigated. The mixing performance of the tank was evaluated by means of particle tracking. It was found that the simulations adequately resolved the highly anisotropic fine-scale turbulence generated by the strong interaction between the impeller, the various other internals and the vessel wall at least at the low Reynolds number. The potential significance of the computed flow structures for crystallization performance is briefly noted.

Keywords: agitated tanks; hydrodynamics; CFD; turbulence; large-eddy simulation; crystallization; lattice-Boltzmann.

*Correspondence to:
Dr J.J. Derksen, Multi-Scale Physics Department, Delft University of Technology, Prins Bernhardlaan 6, 2628 BW Delft, The Netherlands.
E-Mail: j.j.derksen@tudelft.nl

DOI: 10.1205/cherd06025

0263–8762/07/
$30.00 + 0.00

Chemical Engineering Research and Design

Trans IChemE,
Part A, February 2007

INTRODUCTION

Mechanically agitated tanks are used in numerous applications in the chemical process industries including chemical reaction and crystallization. They typically contain internals (e.g., impeller blades, baffles, nozzles, heat exchangers) of various sizes. Moreover, they are usually operated under turbulent conditions (at Reynolds numbers often exceeding 1 000 000) to accelerate transport rates and promote uniform process conditions. The size of turbulent eddies in an industrial agitated tank varies from many centimeters down to a few micrometers.

The performance of agitated tanks is influenced by the inevitable spatial and temporal variation of process conditions originating from the localized and time-varying introduction of mechanical energy (in the impeller zone) and the local injection of process streams. The macroscopic variation of process conditions is mainly determined by the large turbulent eddies. However, the performance of processes involving rapid physico-chemical phenomena occurring at fine scales is influenced also by the small turbulent eddies. For example, the product distribution from a set of simultaneous chemical reactions can be strongly influenced by the characteristics of small turbulent eddies. This is because the dynamics of small eddies influence the local instantaneous composition and temperature of the thin contorted reaction zones forming when fluid elements containing reactive species at different concentrations encounter each other. Similarly, in crystallization the size distribution, shape, crystalline structure and purity of the product is affected by the dynamics of small eddies which influence the mass transfer and degree of supersaturation in the immediate vicinity of precipitating and growing crystals. Finally, the dynamics of small eddies influence the relative motion and, consequently, the coagulation and breakup of small particles, droplets and bubbles.

It is clear that the design, scale-up and optimization of industrial agitated tanks requires a thorough understanding of turbulence dynamics and transport phenomena over a wide range of length and time scales. Since fine-scale processes depend non-linearly on the local, fluctuating flow characteristics, realistic modelling requires a detailed turbulence characterization in addition to the time-averaged flow.

A comprehensive experimental characterization of turbulence dynamics and transport in an agitated tank is a very demanding task. Design information in the open literature is incomplete and largely limited to a few geometric configurations and impeller types that are considered standard. However, the geometry of industrial agitated tanks often deviates substantially from the standard geometry. This paper explores the feasibility of using numerical simulations of high spatial and temporal resolution for the detailed characterization of the flow patterns and turbulence dynamics inside impeller-agitated tanks of complex geometry, with a special focus on tank layouts applied in crystallization.

Computational fluid dynamics (CFD) has emerged as a tool for the design and optimization of chemical process equipment. Conventional CFD techniques for the modelling of turbulent flows have focused primarily on the prediction of the average flow patterns. These techniques are based on an averaged form of the Navier–Stokes equation of motion (referred to as the Reynolds-Averaged Navier–Stokes equation or RANS), which requires an estimation of the effect of the turbulence fluctuations on the mean flow (Hanjalić, 1994). For instance, the widely used $k-\varepsilon$ model assumes that turbulence is locally isotropic and is fully characterized by its time-averaged kinetic energy and time-averaged rate of kinetic energy dissipation. However, in order to characterize the small-scale turbulence and its interaction with other phenomena of interest, time-resolved (as opposed to time-averaged) information is required.

The large-eddy simulation (LES) approach resolves the time-dependent and three-dimensional character of most turbulent eddies; it only approximates the effect of the smallest eddies. It is based on a form of the Navier–Stokes equation of motion derived by spatially filtering scales of motion below the spacing of the selected computational grid. Provided that the CFD mesh is sufficiently fine, the sub-grid scales of motion are of a more or less universal nature (Lesieur and Métais, 1996). They can, therefore, be modelled with more confidence than the larger scales of motion, which are more sensitive to the specific flow type under consideration. Consequently, the LES technique provides a more thorough and accurate turbulence characterization than the RANS technique at the expense of a higher computational cost. The required spatial resolution in a LES is dictated by the nature of the subgrid-scale (SGS) eddies. It is commonly assumed that local production and dissipation of turbulent kinetic energy are in equilibrium. In simple turbulent flows (e.g., homogeneous, isotropic turbulence), such equilibrium takes place in the inertial subrange of the turbulence spectrum (Hinze, 1959). As a result, in a LES the wavenumber corresponding to the grid spacing should lie in the inertial subrange.

Eggels (1996) was the first to perform a LES of the flow in a mechanically agitated tank. Derksen and Van den Akker (1999) later extended the simulation technique of Eggels. They also compared simulated and measured phase-resolved flow fields in a baffled tank stirred by a Rushton turbine. The agreement between the simulated and measured distributions of turbulent kinetic energy in the impeller region was excellent, and much better than that typically achieved with RANS-based simulations. This is likely due to the intrinsic ability of the LES to resolve the time-varying nature of flow in a stirred tank. In contrast, the RANS approach cannot clearly distinguish between the coherent periodic fluctuations generated by the impeller and the stochastic fluctuations induced by turbulence.

In this paper the flow of a Newtonian fluid inside a tank of a non-standard geometry was simulated using the simulation method of Derksen and Van den Akker (1999). It uses a lattice-Boltzmann (LB) discretization of the Navier–Stokes equation, primarily because of its high (parallel) computational efficiency in flow domains of complex shape. Parallelization is essential for the feasibility of highly resolved, time-dependent simulations. It has been recommended that future growth in computational power should be sought through increased parallelism, rather than faster processors (Strohmaier *et al.*, 1997). LB schemes are easier to parallelize than e.g., finite volume schemes, which are popular in commercial CFD software. This is because LB schemes involve only local operations. The price for locality, however, is a finite speed of sound, which imposes a restriction on the maximum velocity that can be simulated under nearly incompressible flow conditions. This implies a time step constraint, which is generally more restrictive than that required by explicit finite volume schemes.

The selected geometry was representative of some industrial crystallizers (Randolph *et al*., 1990). The liquid-filled section of the tank was characterized by a high aspect ratio. A Rushton impeller placed close to the tank bottom drove the flow. The tank contained a draft tube, an inlet at the bottom, an outlet through the side wall and baffles in its lower section. The gap between baffles and impeller tip was very small. In this geometry the flow patterns were expected to be more complicated than those in a standard stirred tank due to the stronger interaction between the impeller and closely located stationary boundaries. A sliding mesh technique (widely available in commercial CFD for mixing vessels) applied to the geometry selected here may have difficulties in resolving the flow in the impeller region because of the close proximity of the impeller tip (rotating) and the tip of the baffles (static).

Although in general it is desirable to experimentally validate CFD results, conducting experimental measurements for the industrial flow studied in this paper was not practical. A well-established computational method that has been thoroughly validated for canonical stirred tank flows [e.g., Rushton turbine flow and pitched-blade turbine flow, see Derksen and Van den Akker (1999), and Derksen (2001)] was used to elucidate a flow that is not amenable to direct measurement. We believe CFD has reached a level of maturity to make it a predictive tool that can substantially reduce risk in the design of industrial stirred tanks despite any remaining uncertainties.

Industrial agitated tanks are operated at Reynolds numbers far exceeding those that can be studied in the laboratory. At high Reynolds numbers the flow domain contains regions with a rich, non-equilibrium, fine turbulence structure strongly interacting with the vessel internals. Such high-Reynolds number flows cannot be fully resolved within the bounds of currently available computational power. The effect of spatial resolution on the computed average flow and turbulence

characteristics was investigated by carrying out simulations at three levels of spatial resolution. Scale-up effects were examined by performing simulations at three Reynolds numbers, 14 000, 82 000 and 350 000. Finally, the mixing performance of the crystallizer was evaluated through particle tracking simulations.

The purpose of this paper was to assess the feasibility of LES for industrial flow cases, and to suggest strategies for its application towards modelling physical and chemical phenomena taking place at the micro-scales in crystallization.

SETUP OF THE SIMULATIONS

Flow Geometry

The geometry of the agitated tank is shown in Figure 1, along with the coordinate system that is used throughout this article. The r,ϕ,x-system was attached to the (static) tank. The angular coordinate θ was used to define the angle of an impeller blade with respect to the vertical plane containing the tank inlet and exit tube. Since the impeller had six equally spaced blades, θ ran from 0° to 60°. The Rushton turbine that was placed closely above the ellipsoidal tank bottom had standard dimensions (see e.g., Derksen and Van den Akker, 1999). The thickness of the blades and the disk was equal to $0.006D$. The presence of a shaft through the bottom of the tank was not taken into account in the simulations. The turbine forced fluid into the annular region between the tank wall and the draft tube. In the lower part of the annulus, eight equally spaced baffles effectively damped the fluid rotation induced by the turbine. Close to the top, which under normal operation would be the boiling zone of the crystallizer, the flow reversed and entered the draft tube. The top free surface was approximated in the simulations as a flat, free-slip surface. Inside the draft tube, the flow was mainly directed downwards, towards the impeller.

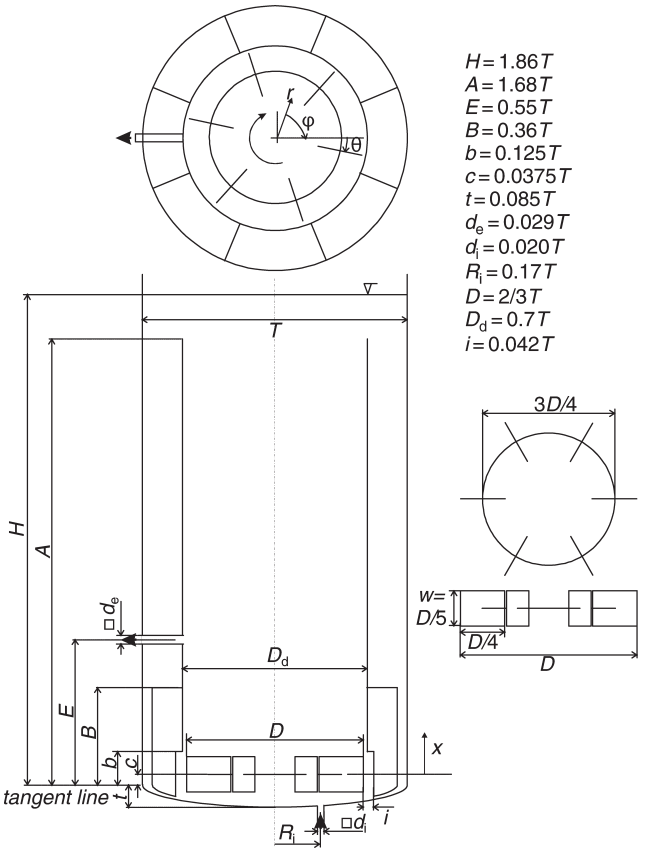

Figure 1. Left: the tank geometry: top view, cross-section through the plane containing the inlet and outlet; right: the Rushton turbine. The squares in front of d_i and d_e denote that these are rectangular channels.

This large-scale recirculating flow system can be characterized by a Reynolds number based on the impeller speed N (in rev s^{-1}) and diameter D:

$$Re = \frac{ND^2}{\nu} \tag{1}$$

where ν is the kinematic viscosity of the fluid (or the effective kinematic viscosity of the crystal slurry).

A feed and an outlet flow were superimposed on the main flow. Fluid was fed into the tank through a nozzle at the bottom, with a (superficial) velocity $0.7{\cdot}v_{tip}$ (v_{tip} being the impeller tip speed, πND). Fluid exited through a nozzle at the side wall that penetrated into the draft tube. The flow rate induced by the impeller was much larger than the feed flow rate.

Simulation Procedure

The simulation procedure has been discussed by Derksen and Van den Akker (1999). The Navier–Stokes equation was discretized according to a LB scheme. In a LB scheme, a simplified kinetic model for a Newtonian fluid is constructed that consists of a set of particles residing at the vertices of a uniform, cubic lattice, and having a discrete velocity distribution. During a single time step, the particles move from lattice site to lattice site and collide. It can be demonstrated that with suitable collision rules and lattice symmetry, the macroscopic behavior of the system resembles that of a real, Newtonian fluid, i.e., the system realizes solutions of the Navier–Stokes equation (Frisch *et al.*, 1986; Chen and Doolen, 1998). The specific scheme that was used in the present work is due to Somers (1993) and Somers and Eggels (1995). It has second order accuracy in space and time.

The effect of subgrid-scale turbulence on the resolved flow was accounted through a Smagorinsky model with $c_s = 0.12$ (Smagorinsky, 1963). The Smagorinsky constant c_s is the ratio between the mixing length and the lattice spacing. It can be shown that for equilibrium turbulence, when the grid spacing expressed as a wavenumber lies in the inertial subrange, c_s should be equal to 0.17. For shear-driven turbulence, values of c_s in the range between 0.06 and 0.12 have been reported [e.g., Moin and Kim (1982) used $c_s = 0.065$ for channel flow; Eggels (1994) found reasonable results for a cylindrical pipe flow with c_s in the range 0.08–0.12]. The value of 0.12 was chosen because it showed good results in previous simulations of stirred tank flow (Derksen and Van den Akker, 1999). Wall damping of the eddy viscosity was not taken into account. The Smagorinsky model does not allow for backscatter from small to larger scales. Backscatter, which mainly influences the fine flow structures, can be resolved by dynamic models (Germano *et al.*, 1991) at high computational cost due to very fine grids needed to facilitate a two-level filtering, especially in the absence of homogeneous flow directions. A 'cheap'

dynamic model known as the mixed-scale model (MSM) due to Sagaut *et al*. (2000) has also been implemented in our computer code. It is known to be less dissipative than the Smagorinsky model and significantly improved results for strongly swirling flows (Derksen, 2005). We will compare the performance of the two SGS models (MSM and Smagorinsky) for the flow case considered here.

The complicated shape of the flow domain was represented by means of the adaptive forcing technique (also known as immersed boundary method, see e.g., Verzicco, 2004). In this technique, no-slip conditions on either static or moving (i.e., the impeller) boundaries are imposed by a force-field acting on the fluid (Derksen and Van den Akker, 1999). The force-field dynamically adapts itself to oppose the (interpolated) flow velocity deficit at the boundaries. With small time steps this method allows for an effective and accurate way of enforcing no-slip boundary conditions.

Implementation

We apply a uniform, cubic lattice of *nx* cells in the axial (x) direction and $ny = nz$ cells in the lateral directions. Our base-case had $nx = 378$, and $ny = nz = 199$. The spatial resolution in relation to the impeller size, was $D = 128\Delta$, with Δ the lattice spacing. The impeller speed was set such that in lattice units the tip speed of the impeller was $v_{tip} \approx 0.1$. This assures that everywhere the fluid velocity is well below the speed of sound of the LB scheme. As a result the numerical solution satisfies the incompressibility condition. The number of time steps per impeller revolution was set to $1/N = 4000\Delta t$. The viscosity determines the Reynolds number [see equation. (1)]. In the base-case $Re = 1.4 \times 10^4$; i.e., $\nu = 2.92 \times 10^{-4}$ in lattice units. The feed flow through the bottom of the tank was set to a fixed value, relative to the impeller tip speed. A uniform velocity profile with $v_{feed} = 0.7 v_{tip}$ was imposed at the entrance of the inlet nozzle. The Reynolds number associated with the feed flow (based on the nozzle diameter and feed flow velocity) was 0.015 times the impeller Reynolds number. At the end of the exit pipe that protrudes $1d_e$ from the side of the tank a no-variation boundary condition was set. LES requires that the three-dimensional, time-dependent flow equations in the full geometry are solved; no geometrical simplifications or reductions were applied. Next to the base-case, five other cases were considered; their characteristics have been summarized in Table 1 (where the spatial resolution is expressed in terms of the number of lattice spacings spanning the impeller diameter; all other dimensions scale accordingly).

Table 1. Characteristics of the simulation cases.

Case #	*Re*	*Spatial resolution: D* (lattice units)	*SGS model*	*Remarks*
1	1.4×10^4	128	Smag.	Base-case
2	1.4×10^4	80	Smag.	Coarse grid
3	1.4×10^4	160	Smag.	Fine grid
4	1.4×10^4	128	MSM	SGS model variation
5	8.2×10^4	160	Smag.	Higher *Re*
6	3.5×10^5	128	Smag.	Semi-industrial *Re*

The code has been parallelized through domain decomposition. The flow domain was divided into equal subdomains which were assigned to different processing elements (PEs) of a parallel computer. During the propagation phase (when particles move from lattice site to lattice site), particle information that crossed subdomain boundaries was communicated between processors by means of a message-passing tool (MPI in the present implementation, see Snir *et al.*, 1996). In a three-dimensional implementation, only two-dimensional sets (planes) of particles need to be communicated. The parallel efficiency of the code was tested for up to 20 cpu's. The computer code showed excellent speed-up. In some cases the speed-up was superlinear due to cache effects. The base-case was run in parallel on six PEs of a PC cluster built of Athlon 1800+ MHz processors. In such a configuration, a single impeller revolution required some 5 h wall-clock time. The total memory required was 1.3 Gbyte.

RESULTS

Macroscopic Flow

The flow in the vertical plane that contains the inlet and outlet (but no baffles, see Figure 1) for the base-case is shown in Figure 2. The global flow pattern is up-flow in the annulus between the tank wall and the draft tube, and down-flow in the draft tube. Various local recirculation regions can be identified. The first one [A, Figure 2(b)] is located between the impeller disk and the bottom of the tank, partly within the impeller swept volume. The right side of this toroidally shaped region interfered with the feed flow. The strong radial outflow from the impeller induces another recirculation and strong turbulence in the lower part of the annulus [B, Figure 2(b)]. Turbulence 'relaminarizes' significantly along the annulus. Finally, upon entering the draft tube, the flow separates and a recirculation is created at the top of the inner draft tube wall [C, Figure 2(b)]. The presence of this recirculation partly blocks the flow entering the draft tube. This blockage induces relatively high velocities near the center of the draft tube.

The turbulent nature of the flow is obvious from the instantaneous realization given in Figure 2(a). The impeller creates turbulence that extends into the lower part of the annulus. The impingement flow at the top of the draft tube (fluid moving in the inward radial direction) is also strongly turbulent. These observations are quantified in Figure 3(a) that shows the distribution of the resolved phase-averaged turbulent kinetic energy, k, normalized by v_{tip}^2, over the same plane as that depicted in Figure 2 (the other panels in Figure 3 relate to sensitivity to grid resolution and Reynolds number that will be discussed in the next section). The unresolved (SGS) part of k was estimated to be at least two orders of magnitude smaller than the resolved part. The procedure for evaluating phase-resolved and phase-averaged statistics is discussed in Appendix A. This type of averaging includes only the contribution to the kinetic energy from the random velocity fluctuations, as pointed out by Wu and Patterson (1989). Contributions from the deterministic velocity oscillations induced by the impeller motion are excluded. Therefore, the total strength of the fluctuations in the vicinity of the impeller is even stronger than what is suggested in Figure 3. However, it was chosen to only depict the random

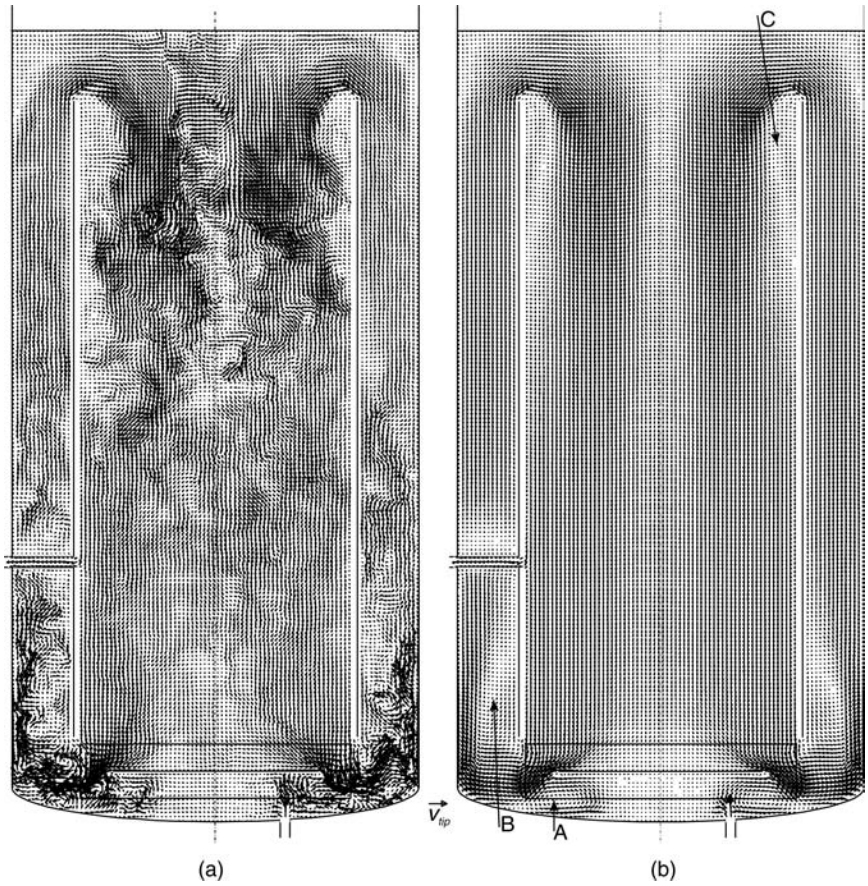

Figure 2. Velocity vectors in the vertical cross-section containing inlet and exit for the base-case simulation. (a) Single flow realization; (b) time-averaged flow. The arrows indicate recirculation regions. The linear grid density of the simulations is twice as high as the density of vectors shown.

kinetic energy for a good comparison of fluctuation levels throughout the tank.

Sensitivity to Grid Resolution, Subgrid-scale Model, and Reynolds Number

Figure 3 compares the turbulent kinetic energy in the vertical cross section containing the inlet and exit tubes for all simulations performed in this work. The most important observation is that sufficient spatial resolution is of crucial importance. Figures 3(a), (b) and (c) have a medium, coarse and fine resolution, respectively. The coarse case has much lower turbulence levels in the impeller outflow and at the impingement zone at the top compared to the two more resolved cases. The medium and the fine cases do not differ very much. There is, however, a consistent trend: the fine case has slightly higher levels of turbulence compared to the medium case. It is especially interesting that the finer the resolution, the deeper turbulence penetrates into the draft tube.

The impact of resolution on the average velocities is shown in Figure 4, which shows velocity profiles at the impeller out-stream for the base case, the coarse and the fine simulation at $Re = 1.4 \times 10^4$. The impeller out-stream profiles are of utmost importance since they drive the flow in the entire tank. From these profiles, and from the turbulent kinetic energy fields (Figure 3) we conclude that the coarse simulation is under-resolved. The medium case (our base-case) and the fine case are in fairly good agreement lending confidence to the results, and allowing us to primarily use the base-case results for further interpreting the flow and the mixing in the crystallizer. The impact of the choice of the SGS model is small. Comparing Figure 3(a) and (d) (Smagorinsky model and mixed-scale model respectively) shows only slightly higher levels of the turbulent kinetic energy for the MSM.

Figure 3(c) and (e) show the Reynolds number effects on the computed turbulent kinetic energy. The turbulent kinetic energy scaled with v_{tip}^2 was slightly more intense for the higher Reynolds number. The Reynolds number mainly affected the small scales of instantaneous flow realizations. Figure 5 shows snapshots of the energy dissipation rate. The higher Reynolds number case contained more energy in finer structures of intense turbulence.

An increase of the Reynolds number to a semi industrial scale value of 3.5×10^5 does not significantly change the macroscopic flow [compare Figures 3(a) and (f)]. At such a high Reynolds number, however, the LES becomes under-resolved (too much kinetic energy in the subgrid-scales), which will affect the quality of the predictions of the micro-scale-related quantities (as the energy dissipation rate). In this study, a wide range of Reynolds numbers was covered

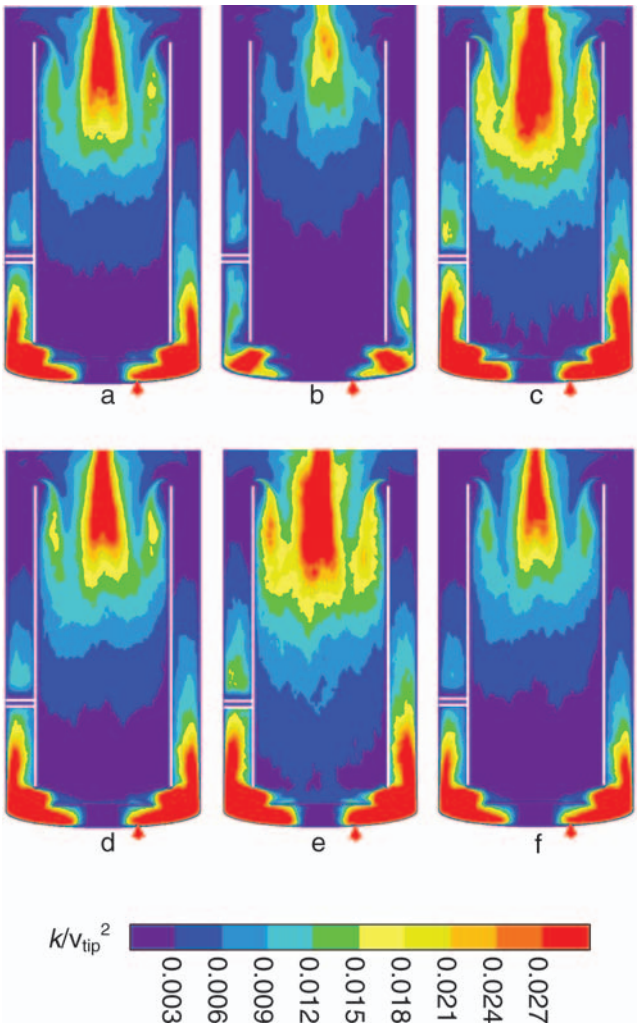

Figure 3. Turbulent kinetic energy levels in the vertical cross section containing inlet (red arrow) and exit. (a): Base-case ($Re = 1.4 \times 10^4$, resolution $D = 128\Delta$, Smag. SGS model); (b): coarser simulation ($D = 80\Delta$); (c): finer simulation ($D = 160\Delta$); (d): same as (a) but now with mixed-scale SGS model; (e) finer simulation at higher Reynolds number ($Re = 8.2 \times 10^4$); (f): same as (a) but now at $Re = 3.5 \times 10^5$. The order of the figures is the same as in Table 1.

to capture the main trends of the Reynolds number effects. These trends are quite valuable in alerting the industrial practitioner about potential changes from pilot-scale performance upon scale-up.

Local Flow

The impeller-generated flow is visualized in the snapshots shown in Figure 6. The wake flow behind the impeller blades had a strong radial component [Figure 6(b)] that determined the pumping capacity of the Rushton turbine. The close proximity of the baffles to the impeller tip complicates the flow compared to the standard Rushton tank, where the impeller usually has a diameter less than 0.5 times the tank diameter and the impeller tip is far away from the baffles. In the space between the baffles a strong turbulent flow was generated. The absolute value of the resolved vorticity [Figure 6(d)] is a useful qualitative indicator for the level of turbulence. The computed levels of (resolved) vorticity in Figure 6(d)

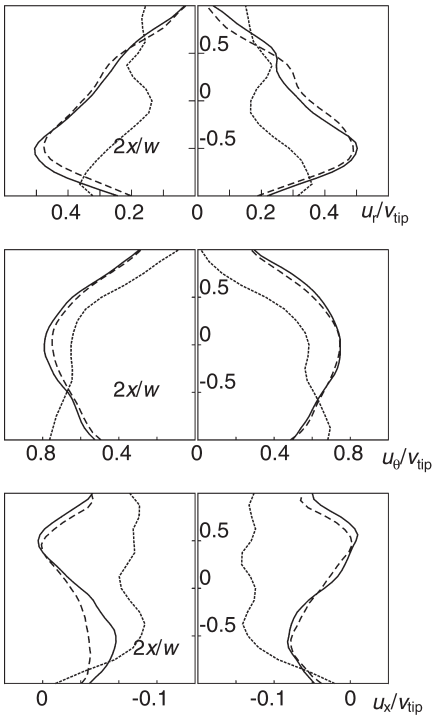

Figure 4. Average velocity profiles at the impeller outstream (at $r = 0.53D$, this is the radial position of the draft tube) in the plane containing inlet and outlet. Left and right graphs correspond to left and right from the impeller in Figure 2. From top to bottom: radial velocity, tangential velocity, axial velocity. Solid curve: high resolution, dashed curve: medium resolution (base-case), dotted curve: low resolution. The axial position is scaled with the impeller blade width w (see Figure 1).

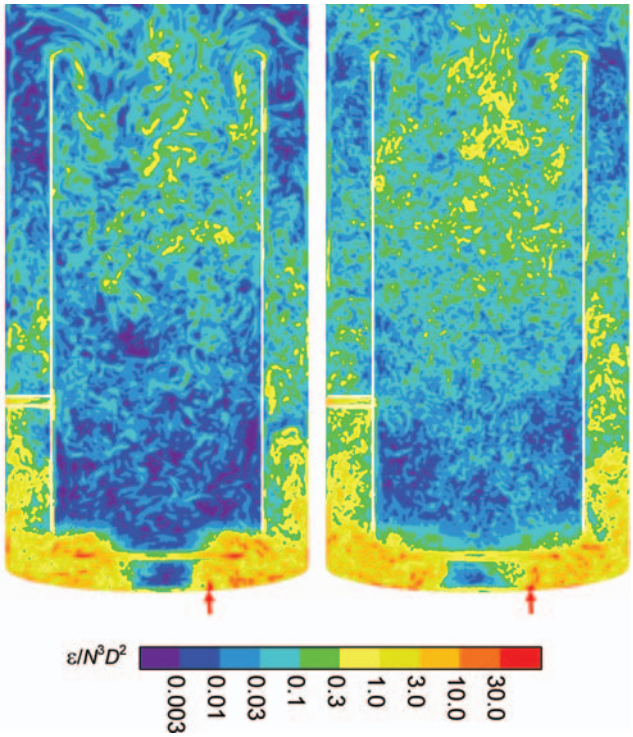

Figure 5. Energy dissipation rate in the vertical cross section containing inlet (red arrow) and exit. Left: fine simulation ($D = 160\Delta$) with $Re = 1.4 \times 10^4$; right: fine simulation at $Re = 8.2 \times 10^4$.

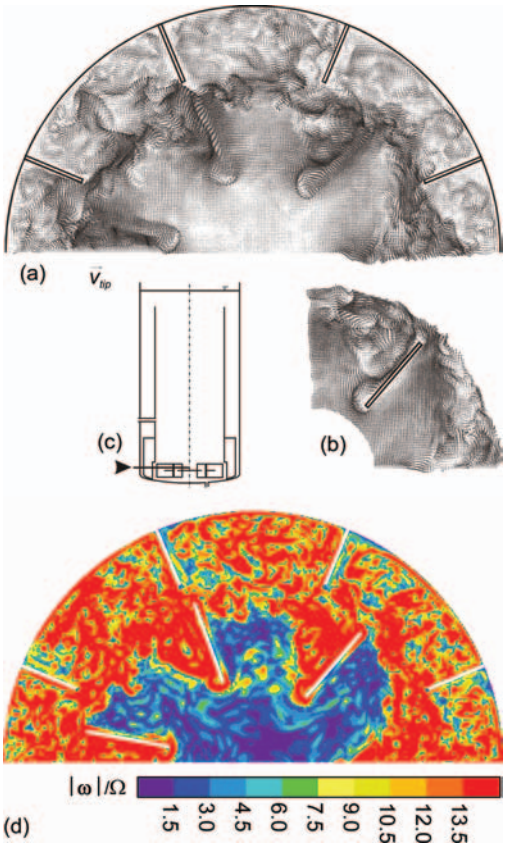

Figure 6. Instantaneous realization of velocity vectors projected on to the horizontal plane at $x = 0.05D$ [as indicated in (c)] for the case #3 (see Table 1). (a) Flow in a static frame of reference. (b) The flow relative to the impeller. (d) The absolute value of the resolved part of the vorticity vector.

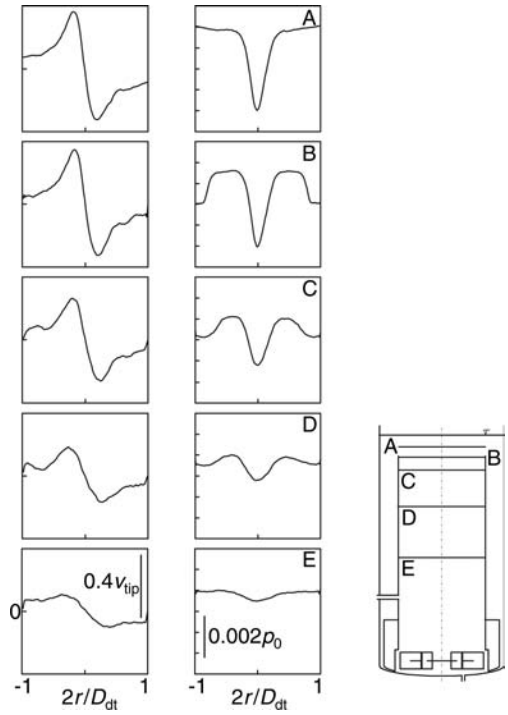

Figure 7. Phase-averaged profiles of the tangential velocity (left), and the static pressure (right) within the draft tube for the base-case. The axial locations of the profiles are indicated in the schematic of the tank.

depend on the cut-off frequency of the LES, because (as in reality) a large part of the vorticity resides with the fine scales. Figure 6(d) shows a sharp distinction between the weakly turbulent draft tube flow (the blue region) that enters the impeller-swept volume from the top and the highly turbulent wakes behind the impeller blades and behind the baffles. Capturing such non-uniformities in the flow character, the significance of which can only be clearly appreciated in connection to a specific crystallization process, is a unique strength of LES.

The baffles in the lower part of the annulus break, but not completely damp, the swirling motion induced by the impeller. The remainder of the swirling motion reaches the top of the annulus and is strongly amplified as the flow turns and moves radially towards the center of the vessel before it enters the draft tube. The resulting high swirl levels and associated pressure profiles are shown in Figure 7. In evaporative crystallizers such swirl my lead to vapour accumulation in the center top region. Deeper into the draft tube the swirl gradually dissipates (Figure 7).

Mixing

In order to assess the mixing performance of the crystallizer, fluid elements (particles) were tracked in the base-case simulation. At every time step, 15 particles were released randomly in the inlet nozzle at the bottom of the tank (15 particles per time step implies 60 000 particles per impeller revolution). The particle positions $\mathbf{x_p}$ were updated according to

$$\frac{d\mathbf{x_p}}{dt} = \mathbf{v_f} \tag{2}$$

where the local time-dependent fluid velocity, $\mathbf{v_f}$, was composed of a resolved part and a subgrid-scale part.

The resolved component of the velocity at the instantaneous particle location was evaluated by interpolating the computed velocity values at the grid nodes according to a second-order interpolation scheme. Equation (2) was integrated according to a first order Euler implicit scheme using the same time step as the LB algorithm (4000 time steps in one impeller revolution for the base-case). Although a higher order interpolation scheme is needed for accurate evaluation of single-and, especially, two-particle Lagrangian statistics (see, e.g., Kontomaris *et al.*, 1992), the lower order scheme used in this work was adequate for a qualitative examination of the particle distribution.

The subgrid contribution to the particle velocity was determined from a Gaussian random process with a standard deviation $u_{sgs} = \sqrt{2/3k_{sgs}}$ representing the SGS motion. The SGS kinetic energy k_{sgs} was estimated based on isotropic, local-equilibrium mixing-length reasoning according to

$$k_{sgs} = C_k c_s^2 \Delta^2 S^2 \tag{3}$$

where C_k is a constant equal to 5 (Mason and Callen, 1986). To have temporal coherency in the SGS motion, a new random velocity was picked after the elapse of a SGS eddy

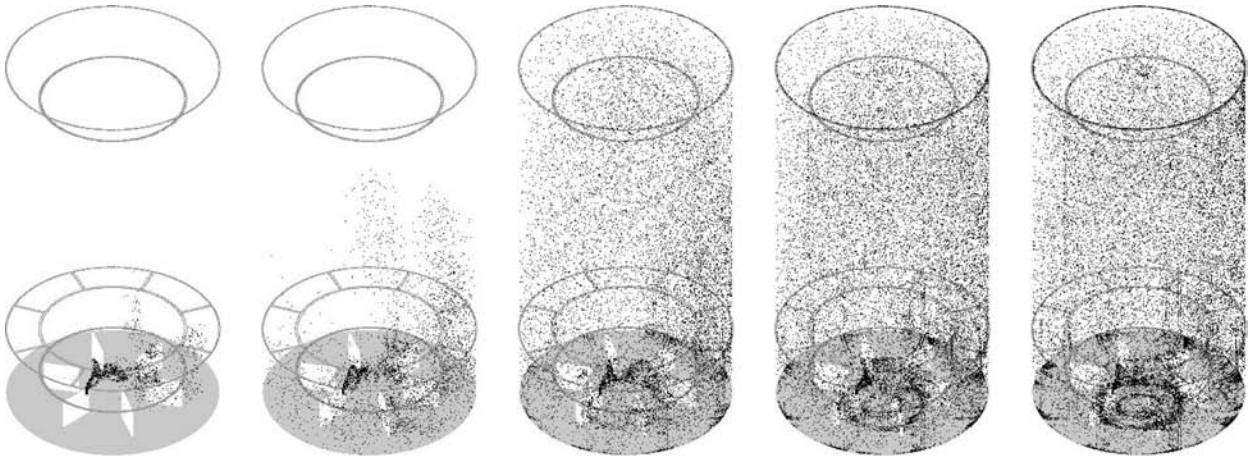

Figure 8. Initial stages of the particle tracking simulations for the base-case. From left to right the time since the introduction of the first particles is 0.5, 1.5, 10, 20 and 30 impeller revolutions respectively. In addition to the particles the graphs show the ellipsoidal bottom of the tank, the impeller blades, and the top level of the baffles, draft tube, and outer tank wall respectively. Only one in 20 particles is displayed.

lifetime $t_{sgs} = C_L(k_{sgs}/\varepsilon)$. with the constant $C_L = 0.15$ (Weber *et al*., 1984), and ε the energy dissipation rate.

Particle tracking simulations were carried out after the tank flow was fully developed. The initial stages of the particle tracking simulation are displayed in Figure 8. When rising through the annulus, the particles have a preference for the angular locations opposite to the feed point, and 90° to the feed point (see the second panel of Figure 8). In later stages the distribution of particles is fairly homogeneous in the part of the tank above the impeller. In the bottom part, particles tend to collect in the corners behind baffles, and in apparently quiescent regions at the bottom.

While travelling through the tank, the residence time of the particles was stored. Figure 9 shows super-positions of the particle locations over selected cross sections through the tank at 10 time instants after the completion of 60 impeller revolutions since the introduction of the first particles. The selected time instants were separated by $\Delta t = 0.01/N$. The particles are coloured according to their residence times. Figure 9 can be viewed as a numerical implementation of

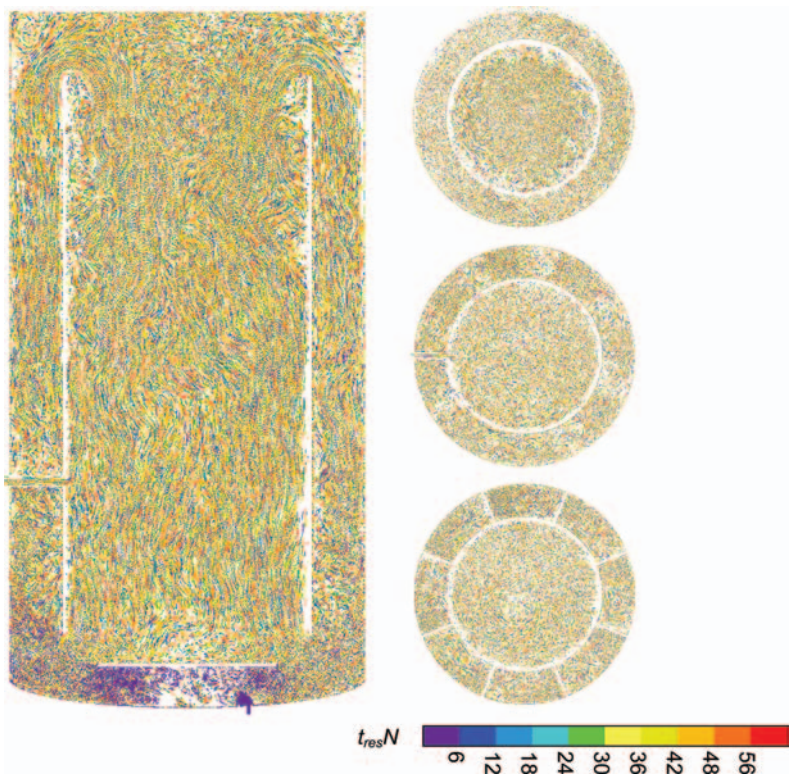

Figure 9. Particles in cross sections with thickness $0.15D$ coloured by their residence time at 10 subsequent moments in time (separated by $\Delta t = 0.01/N$) after approximately 60 impeller revolutions. Left: vertical cross section; right: three horizontal sections at $x = 0.3T$, $0.55T$ and $1.6T$.

the well-known particle-image velocimetry (PIV) technique, which is often used for an experimental characterization of turbulent flows. In terms of the residence time, the system is very homogeneous, except for the part under the impeller where a lot of fresh feed is observed. Also the effect of preferential tangential locations in the annulus can be observed: in the vertical cross section the lower left part of the annulus is slightly more blue than the right part. A consistent picture is given by the lowest horizontal cross section given in Figure 9. The particles in the exit pipe do not have a uniform colour, indicating a broad residence time distribution.

After 60 impeller revolutions the particle concentration field has not reached steady state (i.e., a state with an equal number of particles entering and leaving the tank per unit time). During every impeller revolution 60 000 particles enter the tank, and (after 60 revolutions from start-up) typically 300 leave the tank through the exit pipe. Only when particle concentrations are increased by a factor of 200 (i.e., with about 5×10^8 particles in the tank) may we expect a steady state. Clearly, it is not practical to reach a steady state concentration profile with the particle-based method used here. However, it is still feasible and useful to estimate the residence times of particles in various zones of the flow domain. Moreover, the time scale of the Lagrangian velocity autocorrelation along the trajectories of fluid particles in a zone can be used as a measure of the local micromixing time. Finally, the Lagrangian statistics of particle pairs can be used to quantify the local variance of the concentration field of a dispersing species. The effect of molecular diffusivity can be accounted for by adding a stochastic contribution to the instantaneous particle displacement (Kontomaris and Hanratty, 1994).

The residence time distribution of fluid particles that exited the tank after 60 impeller revolutions is depicted in Figure 10. It is quite uniform. After about five impeller revolutions particles reach the exit pipe. The uniformity of the concentration in the draft tube is then reflected in the uniformity of the residence time distribution.

SUMMARY AND DISCUSSION

In this article we presented results of LES of the turbulent flow in an industrial crystallizer geometry. A parallelized lattice-Boltzmann computer code was employed to reach the high spatial resolutions required. The effect of the grid size was systematically studied. The base-case and the fine case (the latter having roughly twice as many cells as the base-case) showed little difference in terms of the average flow and fluctuation levels, lending confidence to the level of accuracy of the results. Two subgrid-scale models have been applied: the Smagorinsky model and the mixed-scale model. Both gave similar results.

The fine-grid simulation at $Re = 1.4 \times 10^4$ was compared to a simulation on the same grid, but with a much higher Reynolds number (i.e., $Re = 8.2 \times 10^4$). Only slight differences in the turbulent kinetic energy field could be observed, especially in the lower region of the annulus. Comparing snapshots of the flow showed that finer structures are generated by the higher Reynolds number flow as expected (the higher the Reynolds number, the further the turbulence spectrum extends into the high wave-number range). This observation demonstrates that the spatial resolution of the fine grid is sufficient to distinguish between the flow on the small scales at the two Reynolds numbers.

The flow in the crystallizer was driven by a standard Rushton turbine, placed closely above the (dish shaped) tank bottom, and with a small clearance from the baffles. By comparing with the (experimentally and computationally) extensively studied flow induced by a Rushton turbine installed with large bottom and baffle clearances, it was concluded that the proximity to the bottom and to the baffles strongly influences the flow structures in the vicinity of the impeller.

The baffles did not fully damp the swirl. As a result, high swirl levels were encountered in the top of the tank. In normal operation the top part of the tank is a boiling zone and swirl could induce inhomogeneous flow conditions there with vapour concentrating in the high-swirl regions.

Particle tracking simulations were undertaken to evaluate the mixing performance of the tank. They showed that after some five to 10 impeller revolutions uniform conditions are reached (in terms of concentration and residence time of the injected fluid elements), except for the bottom region that is characterized by the presence of fresh feed.

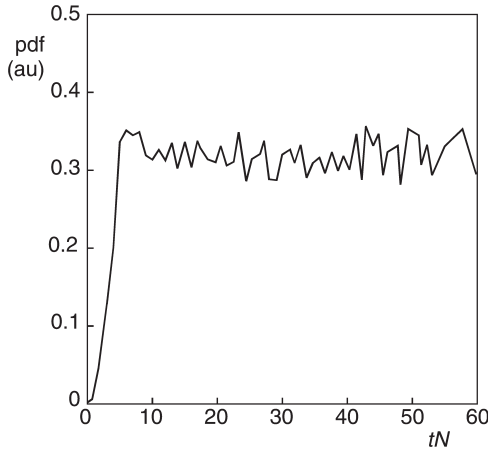

Figure 10. Residence time distribution after 60 impeller revolution of the particles that have exited the tank.

THE ROLE OF HYDRODYNAMICS IN CRYSTALLIZATION

The ultimate goal in modelling crystallization is to predict (trends in) product quality (i.e., crystal size distribution, morphology, purity and so on) as a function of process conditions. Relevant sub-processes directly related to crystallization are primary nucleation, crystal growth, attrition (as a source of secondary nucleation), agglomeration, and boiling (in evaporative crystallization). A fully coupled, direct simulation of all sub-processes involved is not feasible in the foreseeable future, since these processes cover a broad spectrum of time and length-scales. A multi-scale approach that retains as much detail as possible, and allows for realistic coupling between the scales is the best we can do at this moment. It was demonstrated that fluid dynamics can affect phenomena at all scales.

At microscopic scales, the local, time-dependent turbulent energy dissipation rate determines the outcome of the mixing-sensitive competition between nucleation and growth in zones of high super-saturation. This mixing sensitivity becomes even more pronounced in cases of

concomitant nucleation of polymorphs (Ono *et al.*, 2004). The distribution over the various polymorphs that are produced then might depend on small-scale fluctuations in the super-saturation, induced by e.g., the intermittent nature of the turbulent flow.

Crystal-crystal collisions are a source of agglomeration or attrition (depending on the size, and relative velocity of the colliding crystals, and the local degree of super-saturation). In turbulent flows, collisions are mainly driven by local shear. Mei and Hu (1999) demonstrated that the anisotropy of the small-scale flow has significant impact on the collision rate. They showed that the collision rate (N_c) of mono-disperse, spherical particles with diameter d_p in a highly sheared (i.e., anisotropic) homogeneous turbulent flow could increase by a factor of 5 compared to the isotropic estimate of Saffman and Turner (1956):

$$N_c = 0.1618 d_p^3 \left(\frac{\varepsilon}{\nu}\right)^{1/2} n^2 \tag{4}$$

where n is the particle number concentration, ε the energy dissipation rate and ν fluid viscosity. In Figure 11 we show the extent of anisotropy of the flow in terms of the distance from the isotropic state $|A| = \sqrt{(A_2^2 + A_3^2)}$ with A_2 and A_3 the two non-zero invariant of the anisotropy tensor $a_{ij} = (\overline{u_i u_j})/k - 2/3\delta_{ij}$ (Derksen *et al.*, 1999). Among other locations, the feed zone, where supersaturated feed could be entering the vessel, is highly anistropic. In turbulent flows with particles being of the same size or bigger than the Kolmogorov scale, a multi-scale approach to assess the effects of collisions is a versatile one (Ten Cate *et al.*, 2001, 2004).

Finally, the local flow around impeller blades, along with the inertia of the crystals determines the rate at which crystal-impeller collisions occur (Derksen, 2003). These are considered to be a major source of secondary nucleation (Gahn and Mersmann, 1999).

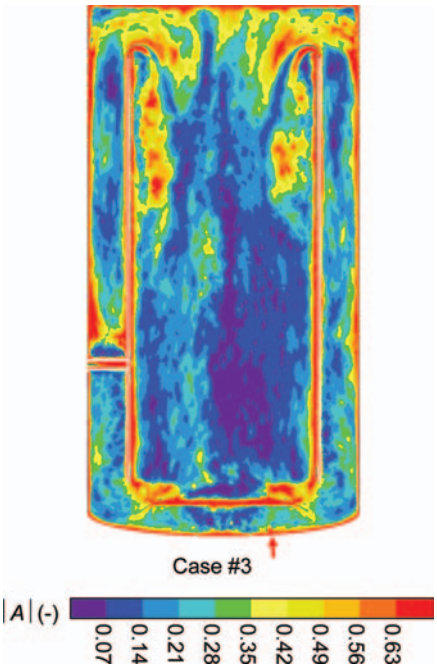

Figure 11. Distribution of the distance to isotropy in the vertical plane containing the inlet and outlet nozzle for simulation case #5.

The macroscopic flow determines the residence times of crystals in the various functional zones in a crystallizer. Local large-scale secondary flows (e.g., back-mixing and short-circuiting between zones) might be affecting the overall flow pattern of a crystallizer. Identifying (and subsequently avoiding) unwanted secondary flow patterns may lead to the design of crystallizers in which all product particles more or less follow the same route, in approximately the same amount of time, thereby enhancing product uniformity. LES can provide accurate estimations of residence times in various zones because it resolves the dynamics of the larger turbulent scales that mostly control dispersion.

It has been assumed in the previous discussion that the effect of crystals on the liquid phase turbulence is minimal. The validity of this assumption should be evaluated especially for cases of high loadings of crystals of large sizes and densities that differ substantially from that of the mother liquid.

ACKNOWLEDGEMENTS

We acknowledge the support and facilities of the National Center for Supercomputing Applications at the University of Illinois at Urbana, Illinois, USA. J.B.M. acknowledges support from the United States Department of Energy under contract DE-FG02-88ER13919.

REFERENCES

Chen, S. and Doolen, G.D., 1998, Lattice Boltzmann method for fluid flows, *Annu Rev Fluid Mech*, 30: 329–364.

Derksen, J.J., 2001, Assessment of large eddy simulations for agitated flows, *Chem Eng Res Des, Trans IChemE, Part A*, 79(A): 824–830.

Derksen, J.J. and Van den Akker, H.E.A., 1999, Large eddy simulations on the flow driven by a Rushton turbine, *AIChE J*, 45: 209–221.

Derksen, J.J., Doelman, M.S. and Van den Akker, H.E.A., 1999, Three-dimensional LDA experiments in the impeller region of a turbulently stirred tank, *Exps Fluids*, 27: 522–532.

Derksen, J.J., 2003, Numerical simulation of solids suspension in a stirred tank, *AIChE J*, 49: 2700–2714.

Derksen, J.J., 2005, Simulations of confined turbulent vortex flow, *Comp & Fluids*, 34: 301–318.

Eggels, J.G.M., 1994, Direct and large-eddy simulation of turbulent flow in a cylindrical pipe geometry, PhD Thesis, Delft University of Technology.

Eggels, J.G.M., 1996, Direct and large-eddy simulations of turbulent fluid flow using the lattice-Boltzmann scheme, *Int J Heat Fluid Flow*, 17: 307–323.

Eggels, J.G.M. and Somers, J.A., 1995, Numerical simulation of free convective flow using the lattice-Boltzmann scheme, *Int J Heat Fluid Flow*, 16: 357–364.

Frisch, U., Hasslacher, B. and Pomeau, Y., 1986, Lattice-gas automata for the Navier-Stokes equation, *Phys Rev Lett*, 56: 1505–1508.

Gahn, C. and Mersmann, A., 1999, Brittle fracture in crystallization processes Part A. Attrition and abrasion of brittle solids, *Chem Eng Sci*, 54: 1273–1282.

Germano, M., Piomelli, U., Moin, P. and Cabot, W., 1991, A dynamic subgrid-scale eddy-viscosity model, *Physics Fluids A*, 3: 1760–1765.

Hanjalić, K., 1994, Advanced turbulence closure models: a view of current status and future prospects, *Int J Heat Fluid Flow*, 15: 178–203.

Hinze, J.O., 1959, *Turbulence* (McGraw-Hill, New York, USA).

Kontomaris, K., Hanratty, T.J. and McLaughlin, J.B., 1992, An algorithm for tracking fluid particles in a spectral simulation of turbulent channel flow, *J Comp Phys*, 103: 231–242.

Kontomaris, K. and Hanratty, T.J., 1994, Effect of molecular diffusivity on point source diffusion in the center of a numerically simulated turbulent channel flow, *Int J Heat Mass Transfer*, 37: 1817–1828.

Lesieur, M. and Métais, O., 1996, New trends in large-eddy simulations of turbulence, *Annu Rev Fluid Mech*, 28: 45–82.
Mei, R.W. and Hu, K.C., 1999, On the collision rate of small particles in turbulent flows, *J Fluid Mech*, 391: 67–89.
Mason, P.J. and Callen, N.S., 1986, On the magnitude of the subgrid-scale eddy coefficient in large-eddy simulations of turbulent channel flow, *J Fluid Mech*, 162: 439–462.
Moin, P. and Kim, J., 1982, Numerical investigation of turbulent channel flow, *J Fluid Mech*, 118: 341–377.
Ono, T., Kramer, H.J.M., Ter Horst, J.H. and Jansens, P.J., 2004, Process modeling of the polymorphic transformation of L-glutamic acid, Crystal Growth & Design, 4: 1161–1167.
Randolph, A.D., Mukhopadhyay, S., Sutradhar, B.C. and Kendal, R., 1990, Double draw-off crystallizer: Major player in the acid rain game? In Myerson, A.S. and Toyokur, K. (eds). *ACS Symposium Series 438, Crystallization as a Separation Process*.
Saffman, P.G. and Turner, J.S., 1956, On the collision of drops in turbulent clouds, *J Fluid Mech*, 1: 2530–2540.
Sagaut, P., Comte, P. and Ducros F., 2000, Filtered subgrid-scale models, *Phys Fluids*, 12: 233–236.
Somers, J.A., 1993, Direct simulation of fluid flow with cellular automata and the lattice-Boltzmann equation, *Appl Sci Res*, 51: 127–133.
Smagorinsky, J., 1963, General circulation experiments with the primitive equations: 1. The basic experiment, *Mon Weather Rev*, 91: 99–164.
Snir, M., Otto, S.W., Huss-Lederman, S., Walker, D.W. and Dongarra J.J., 1996, *MPI: The Complete Reference* (The MIT Press, Cambridge, MA, USA).
Strohmaier, E., Dongarra J.J., Meurer, H.W. and Simon, H.D., 1997, Industrial application areas of high-performance computing, *Lecture Notes Comp Sc*, 1225: 3–10.
Ten Cate, A., Derksen, J.J., Kramer, H.J.M., Van Rosmalen, G.M. and Van den Akker, H.E.A., 2001, The microscopic modelling of hydrodynamics in industrial crystallisers, *Chem Eng Sci*, 56: 2495–2509.
Ten Cate, A., Derksen, J.J., Portela, L.M. and Van den Akker, H.E.A., 2004, Fully resolved simulations of colliding spheres in forced isotropic turbulence, *J Fluid Mech*, 519: 233–271.
Verzicco, R., 2004, Flow in an impeller-stirred tank using an immersed-boundary method, *AIChE J*, 50: 1109–1118.
Weber, R., Boysan, F., Ayers, W.H. and Swithenbank J., 1984, Simulation of dispersion of heavy particles in confined turbulent flows, *AIChE J*, 30: 490–492.
Wu, H. and Patterson, G.K., 1989, Laser-Doppler measurements of turbulent-flow parameters in a stirred mixer, *Chem Eng Sci*, 44: 2207–2221.

The manuscript was received 27 February 2006 and accepted for publication after revision 18 October 2006.

APPENDIX A: COMPUTATION OF PHASE-RESOLVED AND PHASE-AVERAGED STATISTICS

This appendix describes the evaluation of statistical quantities reported in this paper. The following phase-resolved averages in the vertical plane containing the inlet and outlet were updated once the impeller angle reached a new two-degree interval: $\langle u_i\rangle_\theta$, $\langle u_i u_j\rangle_\theta$, $\langle \nu_e\rangle_\theta$, $\langle \nu_e^2\rangle_\theta$, $\langle \nu_e^2(\nu+\nu_e)\rangle_\theta$, $i,j = 1,2,3$. The angular motion of the impeller was of the order of 0.1° per time step, i.e., much smaller than the 2° resolution of the average flow quantities. The brackets $\langle\ \rangle_\theta$ indicate a phase-resolved average at impeller angle θ. Since the average flow in the plane considered is 60° periodic due to the six identical sections the impeller consists of, θ runs from 0° to 60° (with 2° intervals).

From the three moments of the eddy viscosity (ν_e), the average deformation rate $\langle\sqrt{S_{ij}S_{ij}}\rangle_\theta$, the average, subgrid-scale kinetic energy $\langle k_{sgs}\rangle_\theta$, and the average energy dissipation rate $\langle\varepsilon\rangle_\theta$ can be derived:

$$\langle\sqrt{S_{ij}S_{ij}}\rangle_\theta = \frac{1}{c_s}\langle\nu_e\rangle_\theta \tag{A1}$$

$$\langle k_{sgs}\rangle_\theta = 0.05\frac{1}{c_s^2}\langle\nu_e^2\rangle_\theta \tag{A2}$$

$$\langle\varepsilon\rangle_\theta = \frac{1}{c_s^3}\langle\nu_e^2(\nu+\nu_e)\rangle_\theta \tag{A3}$$

Phase-averaged statistics were computed by averaging over all angles. For example, the phase-averaged turbulent kinetic energy k (the distribution of which is shown in Figure 4) was computed as

$$k = \frac{1}{2}\left(\overline{\langle u_i^2\rangle_\theta} - \overline{\langle u_i\rangle_\theta^2}\right) \tag{A4}$$

where the overbar indicates averaging over all angles. The repeated index i in equation (A4) indicates summation.